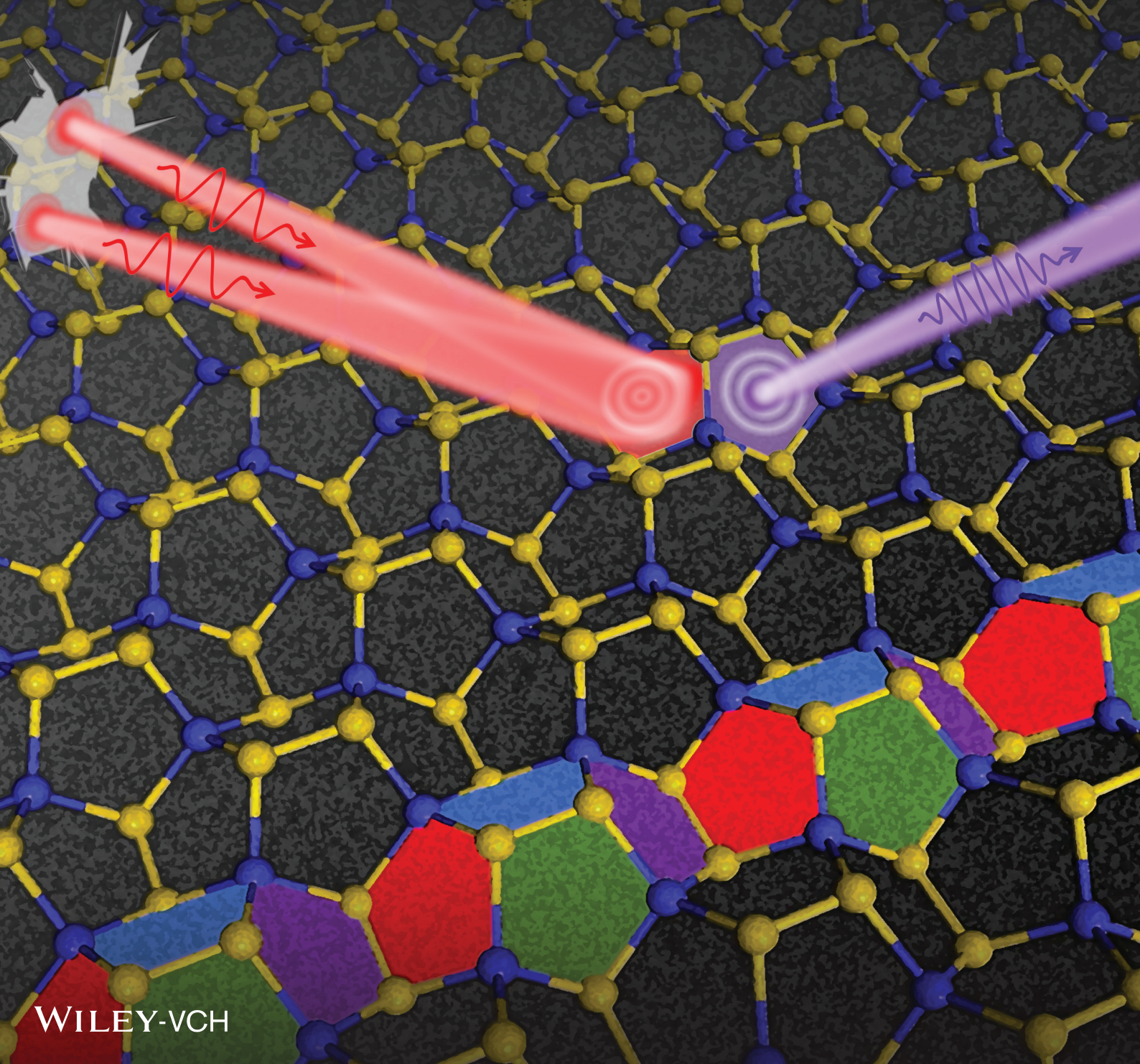


ADVANCED THEORY AND SIMULATIONS



Large Out-of-Plane Second Harmonic Generation Susceptibility in Penta-ZnS₂ Sheet

Yiheng Shen, Yaguang Guo, and Qian Wang*

Second harmonic generation (SHG) of 2D materials has received considerable attention because of the enhanced response to the incident light as compared to that of their bulk counterparts. A significant SHG effect in a new 2D pentagon-based structure of ZnS₂ sheet, penta-ZnS₂, is reported for the first time. On the basis of first-principles calculations combined with global structure search and independent particle approximation, penta-ZnS₂ is found to be dynamically, thermally, and mechanically stable. Unlike most reported 2D materials with only in-plane SHG response, penta-ZnS₂ exhibits giant out-of-plane SHG susceptibility, which is two to three orders of magnitude larger than that of Janus 2D materials, due to the lack of centrosymmetry and out-of-plane mirror symmetry of its geometric structure. The underlying mechanism of the large SHG effect can be applied to other pentagon-based sheets consisting of different elements, thus expanding the family of 2D materials with strong out-of-plane SHG response.

Second harmonic generation (SHG) is a nonlinear optical effect, which has been hotly studied because of its strong response to the incident light as compared to other high order nonlinear optical effects. SHG plays an important role in frequency conversion and nondestructive testing such as upconversion^[1] and the detection of phase transition.^[2] The basic requirement for SHG effect in a material is the breakage of its centrosymmetry, so that the even order terms in electric polarization expansion can exist. For instance, according to Miller's rule ($\chi_{abc} = \chi_{aa}\chi_{bb}\chi_{cc}\Delta_{abc}$),^[3] ferroelectric materials are the potential candidates for second-order nonlinear optics because they have no inversion center, and their first-order polarizations are relatively large. As a consequence, bulk ferroelectric materials, such as KH₂PO₄,^[4] KNbO₃,^[5] and LiNbO₃,^[6] have been found to possess good SHG properties. In recent years, with the rapid development of 2D materials, large SHG responses have been experimentally observed in many 2D non-centrosymmetric materials including 2H-MoS₂,^[7] h-BN,^[8]

2D perovskite,^[9] and CrI₃,^[10] which are much stronger than those of their bulk and few-layered counterparts.^[11] For instance, the SHG susceptibility of 2H-MoS₂ is three orders of magnitude larger than that of bulk MoS₂.^[7] Theoretically, the numerical method for calculating SHG has been well developed by applying the density matrix method within the framework of perturbation theory,^[12,13] which makes it possible to find more 2D materials with SHG effect. For example, lead/tin fluorooxoborates,^[14] GaSe monolayer,^[15] and graphitic ZnS^[16] have been theoretically predicted to exhibit strong SHG effects. However, one common feature of these nonlinear optical materials studied so far is that their SHG responses are confined within the in-plane direction, while the out-of-plane SHG susceptibilities are small^[16,17] or completely lacking^[18]

because of the existence of mirror symmetry in the out-of-plane direction. To date, a successful approach of breaking the out-of-plane mirror symmetry for generating a remarkable out-of-plane SHG signal is to employ the spontaneous electric dipole in Janus nanosheets like α -In₂Se₃ monolayer,^[19] but the preparation of such materials is limited to physical exfoliation or physical vapor deposition.^[20] The direct synthesis of Janus nanosheets from reagents is still beyond current techniques.^[21,22] Therefore, it is highly desirable to theoretically identify new 2D materials that have no out-of-plane mirror symmetry and are feasible for synthesis.

In recent years, 2D materials composed of pure pentagonal structural units have attracted much attention since the theoretical prediction of penta-graphene in 2015.^[23] Numerous new 2D nanosheets constructed exclusively from pentagonal units have been proposed,^[24–31] and some of them have been experimentally synthesized, including penta-PdSe₂^[32–34] and penta-silicene nanoribbons.^[35] Among these pentagon-based sheets, all the penta-graphene-derived structures would exhibit out-of-plane SHG responses because of their unique geometric configurations with neither centrosymmetry nor out-of-plane mirror symmetry. The out-of-plane SHG has been widely used to detect the vertical polarization in 2D materials like Janus transition metal dichalcogenides^[22] and In₂Se₃,^[19] which can realize the ultrafast, noncontact, and noninvasive characterization of lattice structure, chemical bonding as well as stacking order of these 2D nanosheets. In addition, the successful synthesis of such pentagon-based materials^[32–35] suggests that their preparation might be more feasible than that of Janus nanosheets.

Y. Shen, Dr. Y. Guo, Prof. Q. Wang
Center for Applied Physics and Technology
Department of Materials Science and Engineering
HEDPS
BKL-MEMD
College of Engineering
Peking University
Beijing 100871, China
E-mail: qianwang2@pku.edu.cn

 The ORCID identification number(s) for the author(s) of this article can be found under <https://doi.org/10.1002/adts.202000027>

DOI: 10.1002/adts.202000027

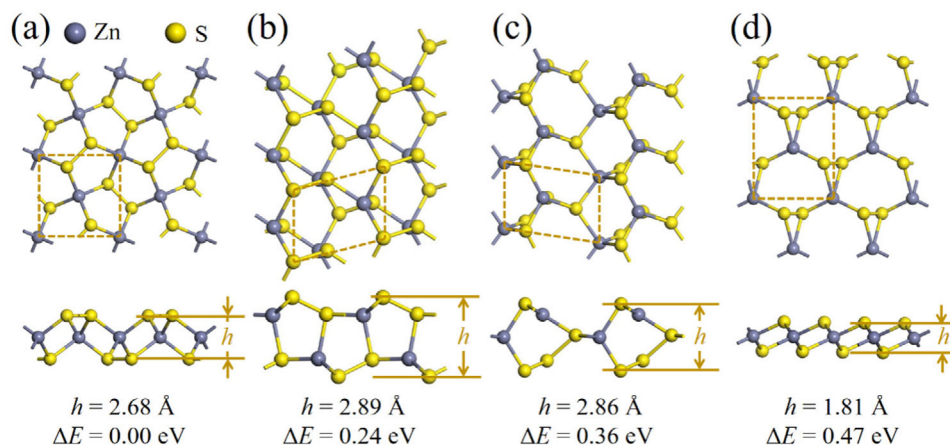


Figure 1. Top and side views, buckling height, and the relative energy per ZnS₂ formula unit of the four energetically low-lying structures of ZnS₂ sheet.

In this work, inspired by the rich nonlinear optical properties of bulk ZnS^[36] and the weak out-of-plane SHG response of its hexagonal 2D allotrope,^[16] we build a penta-graphene-like sheet, named penta-ZnS₂, and perform global structure search combined with state-of-the-art theoretical calculations to confirm the energetic, dynamic, thermal, and mechanical stability of this new structure. We show that penta-ZnS₂ exhibits strong out-of-plane SHG response, differing from other 2D materials with strong in-plane SHG.

First-principles calculations based on density functional theory are carried out by using the Vienna ab initio simulation package (VASP),^[37,38] where the projected augmented wave method^[39] is used to describe electron–ion interactions, and the generalized gradient approximation^[40] with the Perdew–Burke–Ernzerhof (PBE) functional^[41] is used for the exchange–correlation. The Heyd–Scuseria–Ernzerhof (HSE06) hybrid functional^[42,43] is further used to obtain an accurate electronic structure. The k -point sampling for integration in the first Brillouin zone is set as $11 \times 11 \times 1$ for geometry optimization, and $25 \times 25 \times 1$ for electronic structure calculations. The energy cutoff and the convergence thresholds of total energy and inter-atomic force are set to 500 eV, 10^{-8} eV, and 10^{-6} eV·Å⁻¹, respectively. A vacuum space of 13 Å is adopted to avoid the interactions between the periodic images along the out-of-plane direction.

Global structure search for the ground state configuration of 2D ZnS₂ sheet is carried out with a population size of 30 for 30 generations by using the particle swarm optimization method within the evolutionary scheme as implemented in the Crystal structure AnaLYsis by Particle Swarm Optimization (CALYPSO) code,^[44,45] and over 500 initial structures containing up to four formula units of ZnS₂ per cell are generated during the searching process. The phonon property is calculated by using the finite displacement method implemented in the phonopy code,^[46] and the temperature fluctuation in ab initio molecule dynamic (AIMD) simulations is performed by using the Nosé–Hoover thermostat.^[47]

The SHG susceptibility tensor $\chi^{(2)}(-2\omega, \omega, \omega)$ is calculated by using the package developed by Zhang’s group^[48] based on the independent particle approximation,^[12,49] where the SHG tensor is evaluated by the sum of the pure interband contributions χ_e and mixed interband and intraband processes χ_i , both of which

can be deduced from the electronic structure. The details can be found in Text S1, Supporting Information. The electronic structure for the above calculations is obtained at the PBE level with a dense k -point sampling of $99 \times 99 \times 1$. In addition, to compensate for the underestimated band gap at this level, the difference between the band gaps at the PBE and HSE06 levels is applied to the scissors correction in the SHG calculations.^[17,50] For all the components of SHG susceptibility tensor calculated, the errors caused by the ill-defined in-plane intensity of polarization and out-of-plane electric field in the 3D lattice of a 2D material can be cancelled out (see Text S2, Supporting Information for more details).

We fit Zn and S atoms in the penta-graphene structure^[23] by replacing the sp^3 and sp^2 hybridized C atoms with Zn and S atoms, respectively, leading to the atomic ratio of Zn to S being 1:2. As shown in Figure 1a, the optimized structure of ZnS₂ remains the pentagonal configuration with a tetragonal lattice (P-42₁m, space group no.113) and lattice parameters of $a = b = 5.07 \text{ \AA}$, where each unit cell contains two Zn and four S atoms at the Wyck-off positions 2b (0, 0, 0.5) and 4e (0.147, 0.647, 0.589), respectively. We call it penta-ZnS₂. The optimized Zn–S and S–S bond lengths in penta-ZnS₂ are 2.36 and 2.10 Å, which are comparable to those in bulk ZnS and S₈ molecule, respectively. In this structure, there is neither centrosymmetry nor out-of-plane mirror symmetry because of its special geometry with the four-fold coordinated Zn atoms in the middle and the three-fold coordinated S dimers above and below.

To confirm the energetic stability of penta-ZnS₂, we perform global structure search with the formula ZnS₂ by using the CALYPSO code,^[44,45] where over 500 initial structures are generated via the particle swarm optimization algorithm and optimized to their local minimums on the potential energy surface. The energetically low-lying structures and their relative energies (ΔE) with respect to the lowest energy configuration of ZnS₂ sheet are plotted in Figure 1b–d. They all are bulked 2D nanosheets with buckling heights varied in a range of 1.81–2.89 Å, where the Zn atoms are four-fold coordinated and separated by the sulfur atoms. Penta-ZnS₂ is found to be the energetically most stable configuration with its total energy lower by 0.24, 0.36, and 0.47 eV per formula unit than the other three configurations, respectively. To understand the energetic stability of penta-ZnS₂,

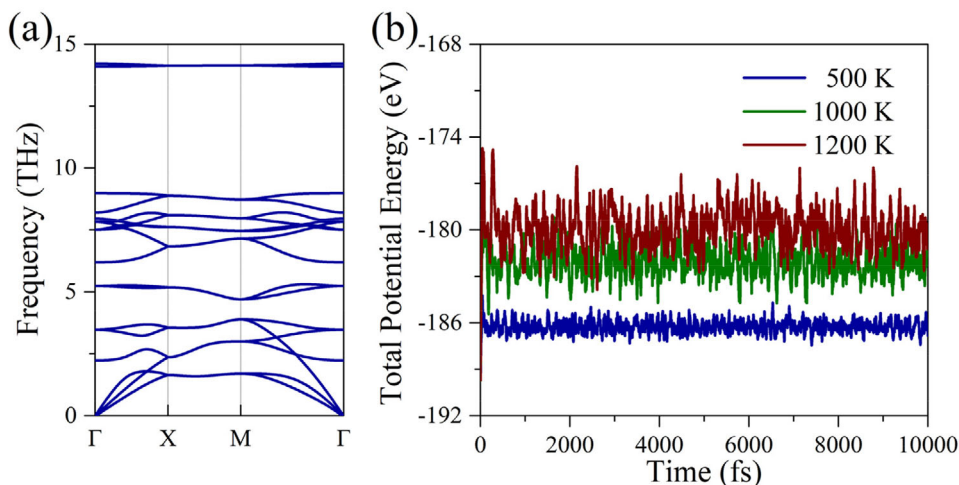


Figure 2. a) Phonon spectrum of penta-ZnS₂. b) Energy fluctuations of penta-ZnS₂ during AIMD simulations at different temperatures.

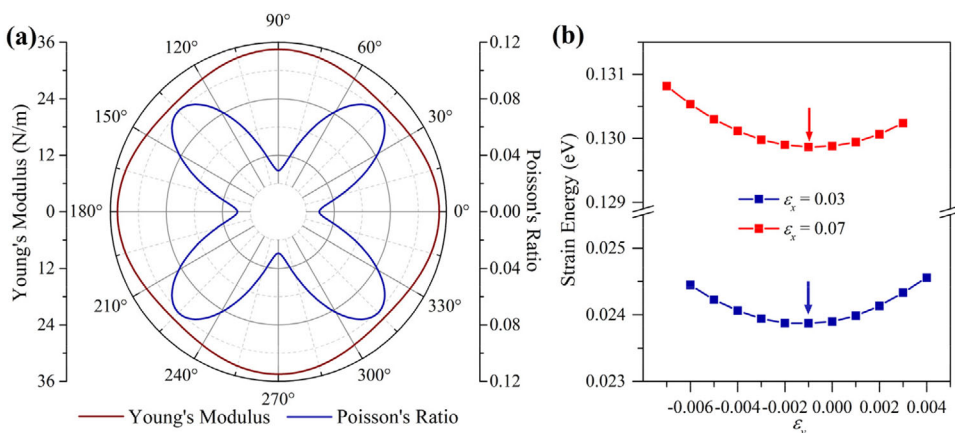


Figure 3. a) Young's modulus and Poisson's ratio of penta-ZnS₂ with respect to stress orientation. b) Strain energy with respect to lateral strain ϵ_y under different axial strain ϵ_x .

we compare the Zn-S bond lengths and \angle S-Zn-S bond angles in penta-ZnS₂ with those in the other low-lying structures. The results are given in Table S1, Supporting Information. We find that although the Zn-S bond lengths in the four structures are comparable with each other, the nonequivalent bond angles \angle S-Zn-S in penta-ZnS₂ are 108.9° and 110.6°, close to the ideal value (109.5°) of the atoms in sp^3 hybridization, while those of the other structures deviate a lot from the ideal value. Thus, we attribute the high stability of penta-ZnS₂ to the low torsion in its geometry because of the sp^3 hybridization of Zn atoms.

We then examine the dynamical stability of penta-ZnS₂. The lack of imaginary modes in the entire Brillouin zone of the calculated phonon spectrum, as shown in **Figure 2a**, indicates that penta-ZnS₂ is dynamically stable. We then examine the thermal stability of penta-ZnS₂ by performing AIMD simulations at different temperatures. Initially, we carry out the AIMD simulation at 500 K for 10 ps with a time step of 1 fs, using a 3×3 supercell to minimize the fake stability caused by the periodic boundary conditions. The total potential energy during the heating process fluctuates around a constant within a narrow range of ± 1 eV per

super cell, as shown in **Figure 2b**, and no obvious reconstructions are found in the geometry of the supercell at the end of the simulation (see **Figure S1**, Supporting Information), confirming the thermal stability of penta-ZnS₂ at 500 K. The heating temperature is further increased to 1000 and 1200 K, respectively, and the thermal stabilities in both cases are verified. Therefore, penta-ZnS₂ is thermally stable and can withstand temperature up to 1200 K.

We study the mechanical properties of penta-ZnS₂ by calculating its stiffness tensor C . For a 2D tetragonal structure, there are only three nonzero independent components in the stiffness tensor under Voigt notation,^[51] namely $C_{11} = 34.5 \text{ N} \cdot \text{m}^{-1}$, $C_{12} = 1.01 \text{ N} \cdot \text{m}^{-1}$, and $C_{66} = 14.5 \text{ N} \cdot \text{m}^{-1}$. These values meet the requirement of Born-Huang criteria, where $C_{11} > C_{12}$ and $C_{66} > 0$.^[52] Thus, the structure is mechanically stable. The mechanical properties along an arbitrary strain direction are then deduced from the stiffness tensor in that direction C' based on the formula $C' = T^{-1} \cdot C \cdot R \cdot T \cdot R^{-1}$, where T is the tensor rotation matrix and $R = \text{diag}(1, 1, 2)$ bridges the gap between engineering and tensor strain, and the results are presented in **Figure 3a**. The Young's modulus E of penta-ZnS₂ shows little

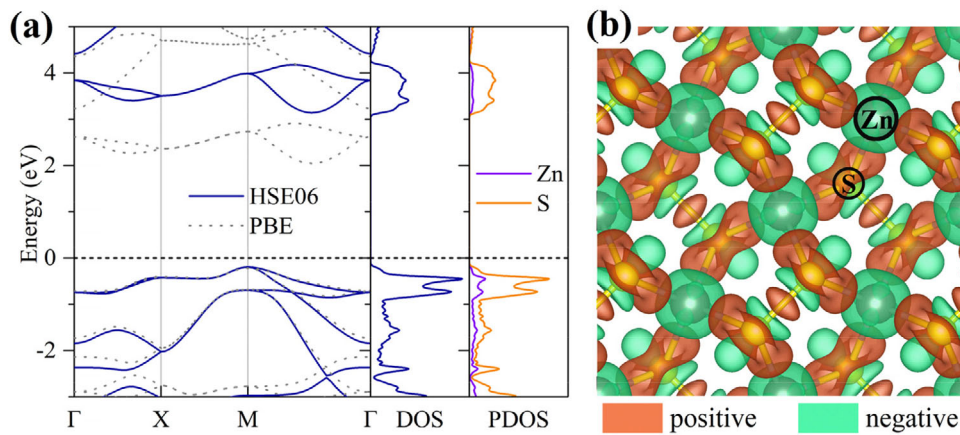


Figure 4. a) Electronic band structure, DOS, and PDOS (the dashed lines for the results at the PBE level), and b) spatial distribution of the deformation charge density (isosurface values = $\pm 0.005 \text{ \AA}^{-3}$) of penta-ZnS₂.

anisotropy, and its maximum is found at the in-plane axial directions, where $E = C_{11} - C_{12}^2/C_{11} = 34.5 \text{ N} \cdot \text{m}^{-1}$, and is only one tenth of that of graphene.^[53] In contrast, the Poisson's ratio ν is highly anisotropic because its minimum is found at the in-plane axial directions, where $\nu = C_{12}/C_{11} = 0.03$, and its maximum value of 0.10 is found at the [110] direction and its equivalents. To confirm the small value of ν at the axial directions, the uniaxial strain of 3% and 7% along the x -axis is applied to the penta-ZnS₂ lattice, and the lateral strain along the y -axis is scanned for the strain energy minimum with a step length of 0.1%. The minimal strain energies in the two cases are found to be 0.024 and 0.130 eV at -0.1% strain, as indicated by the arrows in Figure 3b, confirming the low Poisson's ratio of penta-ZnS₂. The small Young's moduli and low Poisson's ratios along the axial directions could make penta-ZnS₂ a flexible substrate without yielding significant inner stress in heterostructures.

We investigate the electronic properties of penta-ZnS₂ at the HSE06 level. The calculated electronic band structure and density of states (DOS) are plotted in Figure 4a. The band structure calculated at the PBE level is also given for comparison. The indirect band gap of penta-ZnS₂ at the HSE06 level is 3.34 eV, which is 1.08 eV larger than that at the PBE level. In spite of the different values of the band gap, the band dispersions at the two levels are similar, so the scissors-corrected PBE electronic structure can be introduced for calculating SHG susceptibility. The DOS near the Fermi level is contributed from the projected DOS (PDOS) of the Zn and S atoms. As suggested by the spatial distribution of deformation charge density in Figure 4b, covalent bonding exists in the S-S dimers, while Zn—S bonds are predominantly ionic. In fact, using the Bader charge analysis,^[54,55] we find that each Zn atom transfers 0.88 electrons to each of the S₂ dimers.

We evaluate the SHG property of penta-ZnS₂. The four-fold rotary-inversion axis in this structure guarantees a highly reduced SHG susceptibility tensor, allowing only four independent nonzero components $\chi_{xyz}^{(2)} (= \chi_{yxz}^{(2)})$, $\chi_{zxy}^{(2)}$, $\chi_{xcz}^{(2)} (= -\chi_{yzx}^{(2)})$, and $\chi_{zcx}^{(2)} (= -\chi_{zyx}^{(2)})$, which are further abbreviated to $\chi_{14}^{(2)} (= \chi_{25}^{(2)})$, $\chi_{36}^{(2)}$, $\chi_{15}^{(2)} (= -\chi_{24}^{(2)})$, and $\chi_{31}^{(2)} (= -\chi_{32}^{(2)})$ under Voigt notation.^[51] These

tensor components show a crossover between the direction of SHG response and the incident electric field is allowed by the symmetry constraints of this structure, where the in-plane electric field alone contributes to the out-of-plane polarization via $\chi_{36}^{(2)}$ and $\chi_{31}^{(2)}$, and the out-of-plane electric field is also necessary for the in-plane polarization via $\chi_{14}^{(2)}$ and $\chi_{15}^{(2)}$. This symmetry-induced crossover is uncommon in 2D materials.

We deduce the tensor components of the SHG susceptibility of penta-ZnS₂ from its electronic structure at the PBE level. To compensate for the underestimated band gap at this level, the scissors correction of the band gap difference $\Delta = 1.08 \text{ eV}$ is applied to the SHG properties calculations. The nonzero SHG susceptibilities are calculated, and only the SHG signals below the minimal band pair energy of 3.71 eV are considered in the following analysis because of the dominant linear optical absorption beyond this limit. The convergence test of the SHG property with respect to the density of k -points shows that a k -point mesh of $99 \times 99 \times 1$ leads to a good convergent result, as illustrated in Figure S2, Supporting Information. The imaginary parts of the converged nonzero independent SHG susceptibilities are plotted in Figure 5, and their real parts and moduli are plotted in Figure S3, Supporting Information. Unlike previously reported 2D materials with major in-plane SHG response,^[17] penta-ZnS₂ has a stronger out-of-plane SHG response than its in-plane one. Among the four independent SHG susceptibilities, $\text{Im}[\chi_{36}^{(2)}]$ has the most significant peak value of -8.32 pm V^{-1} at 3.19 eV, whose absolute value is about an order of magnitude larger than that of the minor ones. In comparison, the imaginary part of the largest out-of-plane susceptibility $\chi_{31}^{(2)}$ in the buckled ZnS sheet is in the order of 0.01 pm V^{-1} .^[16] The static SHG susceptibilities of penta-ZnS₂ satisfy Kleinman's symmetry,^[19] where only two independent values $\chi_{36}^{(2)}(0) = \chi_{14}^{(2)}(0) = -0.078 \text{ pm V}^{-1}$ and $\chi_{31}^{(2)}(0) = \chi_{15}^{(2)}(0) = 0.044 \text{ pm V}^{-1}$ exist.

Next, we explain the relationship between the electronic structure of penta-ZnS₂ and its SHG susceptibility by tracking the evolution of its density matrix ρ .

$$i\hbar \frac{d\rho}{dt} = [H_0 - \epsilon \mathbf{r} \cdot \mathbf{E}, \rho] \equiv [H_0 + H', \rho] \quad (1)$$

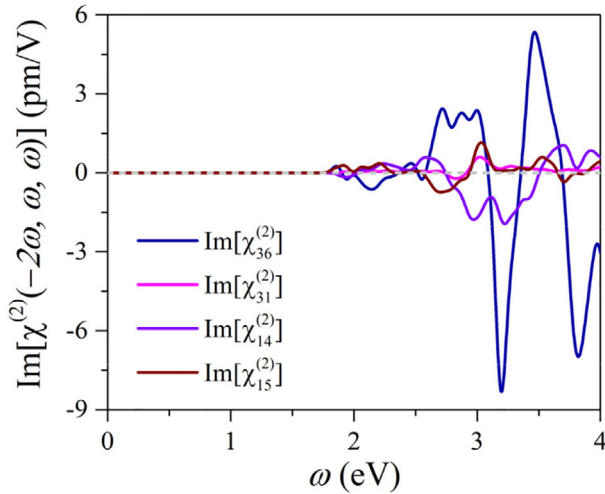


Figure 5. Imaginary part of SHG susceptibility of penta-ZnS₂.

where $H' = -e\mathbf{r} \cdot \mathbf{E}$ is the Hamiltonian for the interaction between the incident electric field and the electrons in materials, and is treated as a perturbation to H_0 . For a crystalline material, the position operator \mathbf{r} originates from the interband-transition term \mathbf{r}_e and the intraband-transition term \mathbf{r}_i . The effect of incident electric field on the density matrix can then be described by the following recursion formula:

$$\frac{\partial \rho^{(n)}}{\partial t} = \frac{1}{i\hbar} \{ [H_0, \rho^{(n)}] + [H', \rho^{(n-1)}] \} \quad (2)$$

where $\rho^{(n)}$ is the n th-order perturbation term of the density matrix ρ under the incident electric field. Thus, $\rho^{(2)}$ for the SHG property is determined by H_0 and $\rho^{(1)}$, namely the band structure and the linear optical response of penta-ZnS₂. $\rho^{(2)}$ can also be distributed to the pure interband transition and mixed interband/intraband transition according to the origin of term \mathbf{r} in H' , which are associated with the interband and intraband contribution to the SHG susceptibilities, respectively.

The contribution from different mechanisms to the imaginary part of both the major SHG susceptibility and the minor ones is presented in Figure 6a–d. The interband and intraband contributions to each SHG susceptibility are comparable in magnitude and tend to oppose each other throughout the examined spectrum. The connection between the SHG property and the linear optical property of penta-ZnS₂ is illustrated by the comparison between the imaginary parts of the SHG susceptibilities and those of the dielectric functions ϵ_{xx} and ϵ_{zz} , which are obtained at the PBE level using the identical k -point mesh and scissors correction in SHG calculations. The calculated results are plotted in Figure 6e,f. The mutual extremums in $\text{Im}[\chi^{(2)}]$ and $\text{Im}[\epsilon(\omega/2)]$ are also marked in Figure 6 by the dashed/dash-dotted lines, where the major peaks of the interband and intraband contributions in a same SHG susceptibility can be related to both $\text{Im}[\epsilon_{xx}(\omega/2)]$ and $\text{Im}[\epsilon_{zz}(\omega/2)]$. Such pattern in the mapping between SHG and linear optics shows in a nutshell how the crossover between the direction of SHG response and the incident electric field works. In the meantime, the connection between the SHG property and the band structure is analyzed by

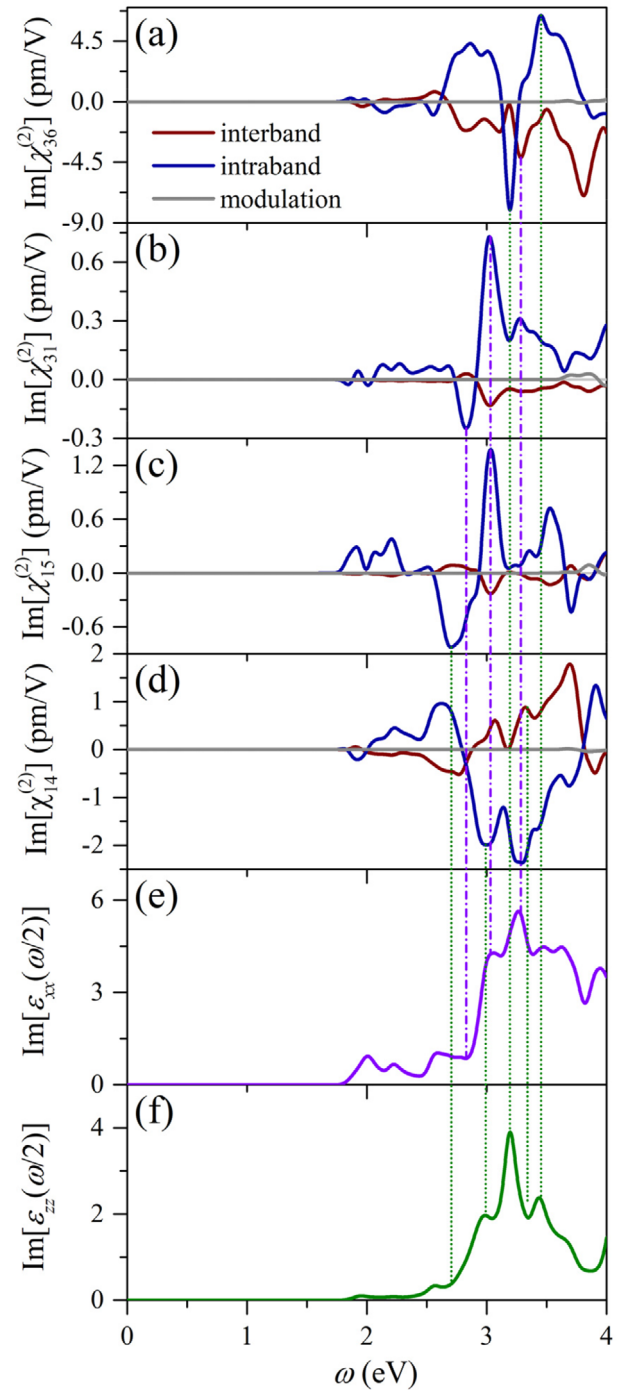


Figure 6. Imaginary parts of the interband, intraband and modulation made contributions to the SHG susceptibility a) $\chi_{36}^{(2)}$, b) $\chi_{31}^{(2)}$, c) $\chi_{15}^{(2)}$, and d) $\chi_{14}^{(2)}$, and dielectric function e) $\epsilon_{xx}(\omega/2)$ and f) $\epsilon_{zz}(\omega/2)$ of penta-ZnS₂.

using the k -point resolved dielectric functions. The peak value of $\text{Im}[\epsilon_{zz}(\omega/2)]$ (3.90 at $\omega/2 = 3.19$ eV) is relevant to that of $\text{Im}[\chi_{36}^{(2)}]$, and mainly contributed from the transitions at the high symmetry point M in the first Brillouin zone, as shown in Figure 7a. The summed-up contribution from all band-to-band transitions

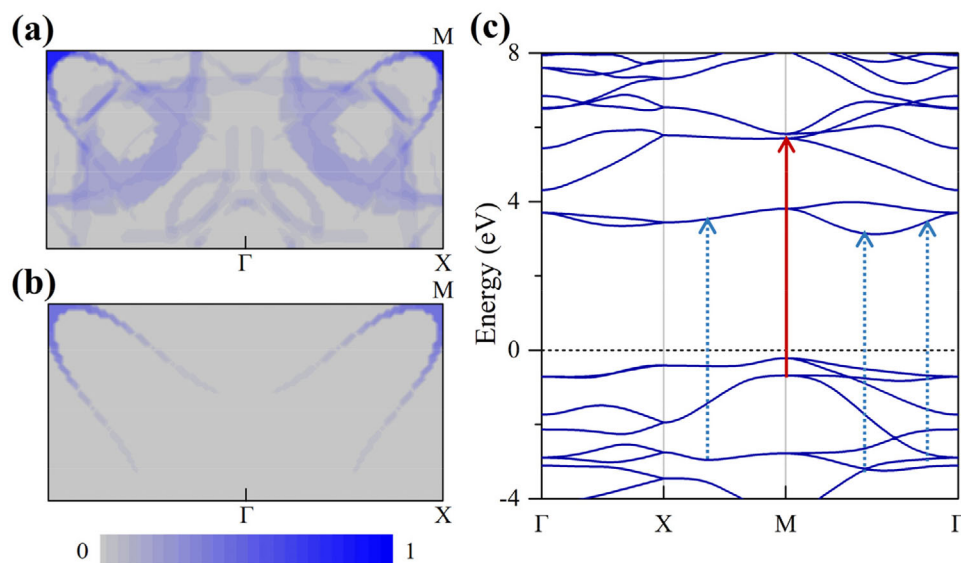


Figure 7. a) Normalized k -point resolved $\text{Im}[\epsilon_{zz}(\omega/2)]$ at the peak value at $\omega/2 = 3.19$ eV; b) the contribution from interband transition VBM-2-CBM+2; and c) band structure of penta-ZnS₂ at the PBE level with scissors correction.

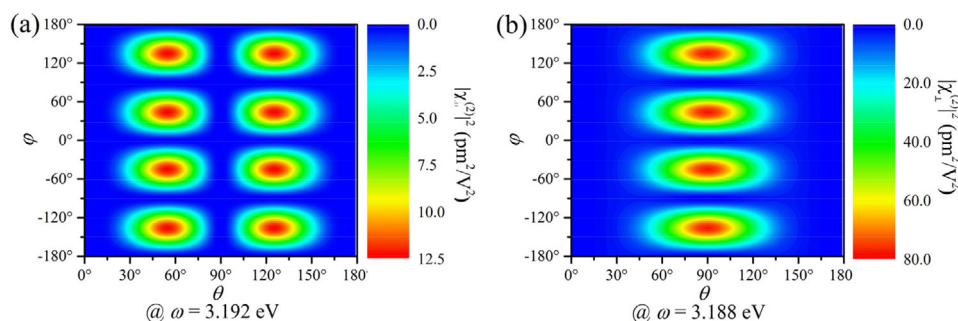


Figure 8. Anisotropic SHG response to the incident electric field along the a) parallel and b) perpendicular directions of penta-ZnS₂.

at each k -point is further decomposed to particular band-to-band transitions, which are plotted in Figure 7b and Figure S4, Supporting Information. The degenerated VBM-2-CBM+2 and VBM-3-CBM+3 transitions at the high symmetry point M, as marked by the red arrow on the scissors-corrected band structure in Figure 7c, are the major contribution to the peak value of $\text{Im}[\epsilon_{zz}(\omega/2)]$. Minor contributions from several other transitions on the high symmetry paths are also noted in dashed blue arrows on the scissors-corrected band structure. It is worth noting that, in the two translations responsible for the major contribution, the excited electron tends to transfer from the negatively charged S atoms to the positively charged Zn atoms, as shown in the band-decomposed charge densities in Figure S5, Supporting Information, implying the polarized Zn—S bonds in penta-ZnS₂ being the origin of its strong out-of-plane SHG susceptibility.

We further evaluate the overall SHG response of penta-ZnS₂. The incident electric field along an arbitrary direction is decomposed into three axial directions denoted by $(90^\circ, 0^\circ)$, $(90^\circ, 90^\circ)$, and $(0^\circ, 0^\circ)$ using spherical coordinate (θ, φ) , respectively. The overall SHG susceptibility is decomposed to $\chi_{||}^{(2)}$ and $\chi_{\perp}^{(2)}$, corresponding to parallel and perpendicular to the incident electric field. The squares of their moduli, written as $|\chi_{||}^{(2)}|^2$ and $|\chi_{\perp}^{(2)}|^2$,

are proportional to the SHG intensity, as shown in Figures 8a and 8b, respectively. Because of the crossover between the directions of the incident electric field and its SHG response, the maxima of $|\chi_{||}^{(2)}|^2$ are found at the incident electric fields along the directions that deviate equally from the three axial directions, where a compromise between the stronger $\chi_{36}^{(2)}$ response at a larger θ and the larger contribution of $\chi_{36}^{(2)}$ to $\chi_{||}^{(2)}$ at a smaller θ is reached. Meanwhile, the maxima of $|\chi_{\perp}^{(2)}|^2$ are found at the incident electric fields along the [110] direction and its equivalents, and is also mainly contributed from $\chi_{36}^{(2)}$.

Using first-principles calculations combined with global structure search and independent particle approximation, we have found that penta-ZnS₂ is the ground state configuration of 2D ZnS₂ nanosheet. The remarkable stability is attributed to its unique structural features with all the Zn atoms in sp^3 hybridization. Penta-ZnS₂ is a semiconductor with an indirect bandgap of 3.34 eV and possesses low Poisson's ratio. More interestingly, different from most 2D materials, penta-ZnS₂ exhibits strong out-of-plane SHG response originating from the breakage of both centrosymmetry and out-of-plane mirror symmetry. Especially, the most significant SHG susceptibility is $\chi_{36}^{(2)}$, which is two to

three orders of magnitude larger than that of Janus 2D materials. These findings demonstrate that penta-graphene-like geometry is a promising structural paradigm for developing 2D materials with strong out-of-plane SHG. We hope that this study can stimulate experimental efforts in exploring nonlinear optical properties of pentagon-based 2D materials going beyond conventional hexagon-based 2D materials.

Supporting Information

Supporting Information is available from the Wiley Online Library or from the author.

Acknowledgements

This work was partially supported by grants from the National Natural Science Foundation of China (Grants No. NSFC-21773004 and NSFC-11974028) and the National Key Research and Development Program of the Ministry of Science and Technology of China (2016YFE0127300 and 2017YFA025003), and was supported by the High Performance Computing Platform of Peking University, China. Y.G. acknowledges the project funded by the China Postdoctoral Science Foundation (No. 2019M650289).

Conflict of Interest

The authors declare no conflict of interest.

Keywords

first-principles calculations, pentagon-based structures, second harmonic generation

Received: February 7, 2020

Revised: March 10, 2020

Published online: March 29, 2020

- [1] N. Thantu, *J. Lumin.* **2005**, *111*, 17.
- [2] L. Bayarjargal, B. Winkler, E. Haussuhl, R. Boehler, *Appl. Phys. Lett.* **2009**, *95*, 061907.
- [3] R. C. Miller, *Appl. Phys. Lett.* **1964**, *5*, 17.
- [4] M. Vallade, *Phys. Rev. B* **1975**, *12*, 3755.
- [5] P. Gunter, *Appl. Phys. Lett.* **1979**, *34*, 650.
- [6] G. D. Boyd, K. Nassau, R. C. Miller, W. L. Bond, A. Savage, *Appl. Phys. Lett.* **1964**, *5*, 234.
- [7] Y. Li, Y. Rao, K. F. Mak, Y. You, S. Wang, C. R. Dean, T. F. Heinz, *Nano Lett.* **2013**, *13*, 3329.
- [8] C. J. Kim, L. Brown, M. W. Graham, R. Hovden, R. W. Havener, P. L. McEuen, D. A. Muller, J. Park, *Nano Lett.* **2013**, *13*, 5660.
- [9] Dong, W. W. L., X. B. Han, Y. Qin, K. Li, W. Li, Z. S. Lin, X. H. Bu, P. X. Lu, *J. Am. Chem. Soc.* **2019**, *141*, 9134.
- [10] Z. Sun, Y. Yi, T. Song, G. Clark, B. Huang, Y. Shan, S. Wu, D. Huang, C. Gao, Z. Chen, M. McGuire, T. Cao, D. Xiao, W. T. Liu, W. Yao, X. Xu, S. Wu, *Nature* **2019**, *572*, 497.
- [11] Y. Wang, J. Xiao, S. Yang, Y. Wang, X. Zhang, *Opt. Mater. Express* **2019**, *9*, 1136.
- [12] J. E. Sipe, E. Ghahramani, *Phys. Rev. B* **1993**, *48*, 11705.
- [13] C. Aversa, J. E. Sipe, *Phys. Rev. B* **1995**, *52*, 14636.
- [14] M. Luo, F. Liang, Y. Song, D. Zhao, N. Ye, Z. Lin, *J. Am. Chem. Soc.* **2018**, *140*, 6814.
- [15] C. Attaccalite, M. Palummo, E. Cannuccia, M. Grüning, *Phys. Rev. Mater.* **2019**, *3*, 074003.
- [16] L. Hu, W. Yi, J. Tang, T. Rao, Z. Ma, C. Hu, L. Zhang, T. Li, *RSC Adv.* **2019**, *9*, 25336.
- [17] H. Wang, X. Qian, *Nano Lett.* **2017**, *17*, 5027.
- [18] M. C. Lucking, K. Beach, H. Terrones, *Sci. Rep.* **2018**, *8*, 10118.
- [19] L. Hu, X. Huang, *RSC Adv.* **2017**, *7*, 55034.
- [20] Y. Zhou, D. Wu, Y. Zhu, Y. Cho, Q. He, X. Yang, K. Herrera, Z. Chu, Y. Han, M. C. Downer, H. Peng, K. Lai, *Nano Lett.* **2017**, *17*, 5508.
- [21] J. Zhang, S. Jia, I. Kholmanov, L. Dong, D. Er, W. Chen, H. Guo, Z. Jin, V. B. Shenoy, L. Shi, J. Lou, *ACS Nano* **2017**, *11*, 8192.
- [22] Y. Lu, H. Zhu, J. Xiao, C. P. Chuu, Y. Han, M. H. Chiu, C. C. Cheng, C. W. Yang, K. H. Wei, Y. Yang, Y. Wang, D. Sokaras, D. Nordlund, P. Yang, D. A. Muller, M. Y. Chou, X. Zhang, L. J. Li, *Nat. Nanotechnol.* **2017**, *12*, 744.
- [23] S. Zhang, J. Zhou, Q. Wang, X. Chen, Y. Kawazoe, P. Jena, *Proc. Natl. Acad. Sci. U. S. A.* **2015**, *112*, 2372.
- [24] X. Li, Y. Dai, M. Li, W. Wei, B. Huang, *J. Mater. Chem. A* **2015**, *3*, 24055.
- [25] Y. Ding, Y. Wang, *J. Mater. Chem. C* **2015**, *3*, 11341.
- [26] H. Liu, G. Qin, Y. Lin, M. Hu, *Nano Lett.* **2016**, *16*, 3831.
- [27] S. Zhang, J. Zhou, Q. Wang, P. Jena, *J. Phys. Chem. C* **2016**, *120*, 3993.
- [28] F. Shojaei, J. R. Hahn, H. S. Kang, *J. Mater. Chem. A* **2017**, *5*, 22146.
- [29] J. Zhao, H. Zeng, *ACS Omega* **2017**, *2*, 171.
- [30] L. Liu, I. Kankam, H. L. Zhuang, *Phys. Rev. B* **2018**, *98*, 205425.
- [31] S. Sun, F. Meng, Y. Xu, J. He, Y. Ni, H. Wang, *J. Mater. Chem. A* **2019**, *7*, 7791.
- [32] D. Oyedele, S. Yang, L. Liang, A. A. Puretzy, K. Wang, J. Zhang, P. Yu, P. R. Pudasaini, A. W. Ghosh, Z. Liu, C. M. Rouleau, B. G. Sumpter, M. F. Chisholm, W. Zhou, P. D. Rack, D. B. Geoghegan, K. Xiao, *J. Am. Chem. Soc.* **2017**, *139*, 14090.
- [33] W. L. Chow, P. Yu, F. Liu, J. Hong, X. Wang, Q. Zeng, C. H. Hsu, C. Zhu, J. Zhou, X. Wang, J. Xia, J. Yan, Y. Chen, D. Wu, T. Yu, Z. Shen, H. Lin, C. Jin, B. K. Tay, Z. Liu, *Adv. Mater.* **2017**, *29*, 1602969.
- [34] E. Li, D. Wang, P. Fan, R. Zhang, Y.-Y. Zhang, G. Li, J. Mao, Y. Wang, X. Lin, S. Du, H.-J. Gao, *Nano Res.* **2018**, *11*, 5858.
- [35] J. I. Cerda, J. Slawinska, G. Le Lay, A. C. Marele, J. M. Gomez-Rodriguez, M. E. Davila, *Nat. Commun.* **2016**, *7*, 13076.
- [36] M. Gruning, C. Attaccalite, *Phys. Chem. Chem. Phys.* **2016**, *18*, 21179.
- [37] G. Kresse, J. Furthmuller, *Phys. Rev. B* **1996**, *54*, 11169.
- [38] G. Kresse, J. Furthmuller, *Comput. Mater. Sci.* **1996**, *6*, 15.
- [39] P. E. Blöchl, *Phys. Rev. B* **1994**, *50*, 17953.
- [40] M. P. Teter, M. C. Payne, D. C. Allan, *Phys. Rev. B* **1989**, *40*, 12255.
- [41] J. P. Perdew, K. Burke, M. Ernzerhof, *Phys. Rev. Lett.* **1996**, *77*, 3865.
- [42] J. Heyd, G. E. Scuseria, M. Ernzerhof, *J. Chem. Phys.* **2003**, *118*, 8207.
- [43] J. Heyd, G. E. Scuseria, M. Ernzerhof, *J. Chem. Phys.* **2006**, *124*, 219906.
- [44] Y. Wang, J. Lv, L. Zhu, Y. Ma, *Phys. Rev. B* **2010**, *82*, 094116.
- [45] Y. Wang, J. Lv, L. Zhu, Y. Ma, *Comput. Phys. Commun.* **2012**, *183*, 2063.
- [46] I. T. Togo, *Scr. Mater.* **2015**, *108*, 1.
- [47] S. Nosé, *J. Chem. Phys.* **1984**, *81*, 511.
- [48] Z. X. Fang, J. Lin, R. Liu, P. Liu, Y. Li, X. Huang, K. N. Ding, L. X. Ning, Y. F. Zhang, *CrystEngComm* **2014**, *16*, 10569.
- [49] S. N. Rashkeev, W. R. L. Lambrecht, B. Segall, *Phys. Rev. B* **1998**, *57*, 3905.
- [50] Z. H. Levine, D. C. Allan, *Phys. Rev. Lett.* **1991**, *66*, 41.
- [51] Y. Le Page, P. Saxe, *Phys. Rev. B* **2002**, *65*, 104104.
- [52] J. Li, X. Fan, Y. Wei, G. Chen, *Sci. Rep.* **2016**, *6*, 31840.
- [53] C. Lee, X. Wei, J. W. Kysar, J. Hone, *Science* **2008**, *321*, 385.
- [54] G. Henkelman, A. Arnaldsson, H. Jónsson, *Comput. Mater. Sci.* **2006**, *36*, 354.
- [55] W. Tang, E. Sanville, G. Henkelman, *J. Phys.: Condens. Matter* **2009**, *21*, 084204.